OPEN BIOLOGY

royalsocietypublishing.org/journal/rsob

Research

Cite this article: Morton CR, Rzechorzek NJ, Maman JD, Kuramochi M, Sekiguchi H, Rambo R, Sasaki YC, Davies OR, Pellegrini L. 2021 Structural basis for the coiled-coil architecture of human CtIP. *Open Biol.* **11**: 210060. https://doi.org/10.1098/rsob.210060

Received: 11 March 2021
Accepted: 5 May 2021

Subject Area:
biochemistry/biophysics/structural biology

Keywords:
human CtIP, DNA repair, coiled-coil structure

Author for correspondence:
L. Pellegrini
e-mail: lp212@cam.ac.uk

†Present address: The Francis Crick Institute, London NW1 1AT, UK.

Electronic supplementary material is available online at https://doi.org/10.6084/m9.figshare.c.5448673.

THE ROYAL SOCIETY PUBLISHING

Structural basis for the coiled-coil architecture of human CtIP

C. R. Morton[1], N. J. Rzechorzek[1,†], J. D. Maman[1], M. Kuramochi[2,3], H. Sekiguchi[4], R. Rambo[5], Y. C. Sasaki[2,3,4], O. R. Davies[6] and L. Pellegrini[1]

[1]Department of Biochemistry, University of Cambridge, Cambridge CB2 1GA, UK
[2]Graduate School of Frontier Sciences, The University of Tokyo, Tokyo, Japan
[3]AIST-UTokyo Advanced Operando-Measurement Technology Open Innovation Laboratory, National Institute of Advanced Industrial Science and Technology, Kashiwa, Japan
[4]Centre for Synchrotron Radiation Research, Japan Synchrotron Radiation Research Institute, Kouto, Sayo-cho, Sayo-gun, Hyogo 679-5198, Japan
[5]Diamond Light Source, Didcot, Oxfordshire OX11 0DE, UK
[6]Institute of Cell Biology, University of Edinburgh, Edinburgh EH9 3BF, UK

NJR, 0000-0003-2068-1424; MK, 0000-0003-1643-3997; HS, 0000-0001-7590-3624; YCS, 0000-0003-3403-237X; ORD, 0000-0002-3806-5403; LP, 0000-0002-9300-497X

The DNA repair factor CtIP has a critical function in double-strand break (DSB) repair by homologous recombination, promoting the assembly of the repair apparatus at DNA ends and participating in DNA-end resection. However, the molecular mechanisms of CtIP function in DSB repair remain unclear. Here, we present an atomic model for the three-dimensional architecture of human CtIP, derived from a multi-disciplinary approach that includes X-ray crystallography, small-angle X-ray scattering (SAXS) and diffracted X-ray tracking (DXT). Our data show that CtIP adopts an extended dimer-of-dimers structure, in agreement with a role in bridging distant sites on chromosomal DNA during the recombinational repair. The zinc-binding motif in the CtIP N-terminus alters dynamically the coiled-coil structure, with functional implications for the long-range interactions of CtIP with DNA. Our results provide a structural basis for the three-dimensional arrangement of chains in the CtIP tetramer, a key aspect of CtIP function in DNA DSB repair.

1. Introduction

Damage to the chemical structure of DNA is a constant threat to the genetic stability of the cell and the faithful transmission of genetic information. In response to DNA damage, complex cellular responses have evolved to signal the presence of genotoxic lesions and activate the appropriate repair pathway [1,2]. Double-strand breaks (DSBs) in the DNA double helix represent a highly dangerous injury that—if left unrepaired—can cause chromosomal rearrangements and genomic instability, a major predisposing factor to the development of cancer and other pathologies. DSBs in eukaryotic cells are normally repaired by two conserved repair mechanisms: non-homologous end joining (NHEJ) [3], which rejoins directly the broken DNA ends with occasional loss of information at the damaged site, and homologous recombination (HR) [4], a high-fidelity mode of repair prevalent during and after DNA replication, when a sister chromatid copy is available as a template for repair.

The choice of DSB repair pathway is influenced by complex cellular mechanisms that depend on the preferred recruitment to the DNA ends of specialized protein factors, which then determine the mode of DSB repair [5–7]. The extent of DNA-end resection is a critical factor in deciding the DSB repair pathway. Resection is normally prevented by the NHEJ end-binding Ku protein and the 53BP1-Rif1-Shieldin complex, which act to channel repair

© 2021 The Authors. Published by the Royal Society under the terms of the Creative Commons Attribution License http://creativecommons.org/licenses/by/4.0/, which permits unrestricted use, provided the original author and source are credited.

towards NHEJ. During the S-phase, the role of the BRCA1-BARD1 complex becomes predominant in promoting extensive resection of DNA ends, thus favouring repair by HR.

CtIP (CtBP-interacting protein)/RBBP8 (retinoblastoma-binding protein 8) was first identified as a transcriptional co-repressor, but accumulating evidence has since established its paramount importance in maintaining genomic stability. Thus, CtIP has a critical role in promoting HR, acting together with BRCA1 and the Mre11-Rad50-Nbs1 (MRN) complex to initiate DNA-end resection [8,9]. Furthermore, CtIP mediates the cell-cycle control of repair choice upon CDK phosphorylation at T847 [10], a post-translational modification (PTM) that is necessary for efficient resection and is shared with its distant yeast orthologue Sae2 [11]. Although its mechanism of action remains poorly understood, current evidence indicates that one important function of CtIP/Sae2 is to activate the endonucleolytic cleavage of blocked DNA ends by the Mre11 nuclease at the start of the resection process [12,13]. In addition to its direct involvement in the process of enzymatic resection of DNA ends, CtIP is a hub for protein–protein interactions, coordinating the recruitment of repair factors to damaged DNA [9]. CtIP is also extensively post-translationally modified, and these PTMs are important for its repair function [9]. Recent evidence further shows that CtIP's role in maintaining genomic stability extends to the stabilization of stalled forks during DNA replication [14–16].

Our mechanistic understanding of the function of CtIP in HR is limited by a lack of structural information. Such information has proved difficult to acquire as CtIP appears to be intrinsically disordered over most of its sequence, with the exception of its alpha-helical N-terminal region [17]. Amino acid conservation points to the presence of functionally important N- and C-terminal domains [18–20] that have been shown to bind DNA and the MRN complex [20–24]. An important mechanistic advance came from the demonstration that CtIP exists in a tetrameric form, due to the presence of a short tetramerization motif at its helical N-terminus [21]. Tetramerization is important for CtIP's repair function, as the single-point mutation L27E that abolishes tetramer formation yields a protein that is deficient in HR [21]. Indeed, conservation of the tetramerization motif in the fission-yeast orthologue Ctp1 [22] reinforces the important functional role of this oligomeric state in DSB repair.

The crystal structure of the tetramerization motif, together with the predicted presence of C-terminally juxtaposed coiled-coil segments, suggested an elongated structure for CtIP, based on the head-to-head association of two parallel coiled-coil dimers [21]. Such an architecture is supported by a recent characterization of full-length human CtIP, showing that the tetrameric protein forms a dumbbell shape, in agreement with the proposed mechanism of tetramerization [25]. The functional implication of such structural arrangement is that CtIP might be able to bridge distinct DNA molecules and to position its conserved functionally important C-terminal domains at distant DNA sites. Biochemical evidence for such bridging behaviour, as well as for the formation of higher-order assemblies, has recently been obtained [26,27].

The tetramerization motif of human CtIP spans amino acids 18–32, while the region with strongly predicted alpha-helical conformation extends to residue 145 (figure 1*a*,*b*). Furthermore, embedded within the coiled-coil region is a zinc-binding motif of unknown structure, where zinc coordination is shared between two conserved cysteine ligands in each chain of the dimeric coiled-coil. Thus, the nature of the three-dimensional architecture of the CtIP N-terminus and how it affects CtIP function remains to be determined. In this paper, we present evidence—drawing on multiple experimental techniques—that the conserved helical sequence of CtIP juxtaposed to its tetramerization motif forms a parallel coiled-coil, providing experimental support for the proposed dimer-of-dimers architecture. Furthermore, we show that the presence of the zinc-binding motif in the middle of the coil allows for the generation of distinct geometries of the CtIP N-terminus.

2. Results

2.1. Crystal structure of the CtIP N-terminal coiled-coil

To improve our understanding of CtIP structure and function, we focused on the region that is juxtaposed to the C-terminus of the tetramerization motif. In keeping with the nomenclature adopted for the CtIP N-terminal domain (NTD) [21], we will refer to this sequence of CtIP as cNTD (C-terminal NTD), to distinguish it from the N-terminal part of the NTD (N-terminal NTD; nNTD), which comprises the tetramerization motif (figure 1*a*,*b*). Constructs designed for crystallization started after leucine 27, which is critical for tetramerization [21], and extended to residue 145, therefore including the entire span of the predicted alpha-helical region. Sparse matrix screening resulted in diffracting crystals for CtIP-cNTD construct 31–145; however, diffraction quality was poor and attempts to improve crystal quality were not successful.

The CtIP-cNTD binds zinc via cysteines C89 and C92 [21]; the zinc-binding motif, thus, interrupts the extended helical sequence of the CtIP-NTD to generate two flanking coiled-coil segments (figure 1*a*,*b*). Zinc binding is shared by the two chains of the CtIP-cNTD dimer (1 zinc:2 cNTD stoichiometry), but it does not play a role in CtIP-cNTD dimerization [21]. We reasoned that sub-stoichiometric incorporation of zinc in recombinant CtIP-cNTD might cause conformational heterogeneity preventing the formation of well-ordered crystals. A double C89A, C92A mutant (Mut) CtIP-cNTD protein was prepared, which crystallized readily and showed improved diffraction properties. We determined its crystal structure at 2.8 Å resolution by molecular replacement (MR), using as search templates two coiled-coil models comprising the strongly predicted coiled-coil regions flanking the zinc-binding motif (electronic supplementary material, figure S1, table S1 and Methods).

The crystal structure revealed that the cNTD region spanning residues 31–136 folds in a highly elongated dimer of uninterrupted parallel alpha helices (figure 1*c*). Within this helical structure, two coiled-coil regions—named here CC-N and CC-C—comprising amino acids V35 to L84 (CC-N) and I117 to L138 (CC-C), flank the zinc-binding site (figure 1*e*,*d*). The coiled-coil structure of both CC-N and CC-C follows largely the expected heptad-repeat pattern of interdigitating hydrophobic residues. The residues surrounding the positions of cysteines 89 and 92, comprising the zinc-binding motif, interrupt the coiled-coil conformation and form instead two alpha helices running parallel to each other in the dimer (figure 1*c*).

The presence of two cysteine ligands per CtIP chain and the observed 2:1 protein-to-zinc stoichiometry [21] had led to the expectation of intermolecular coordination of one

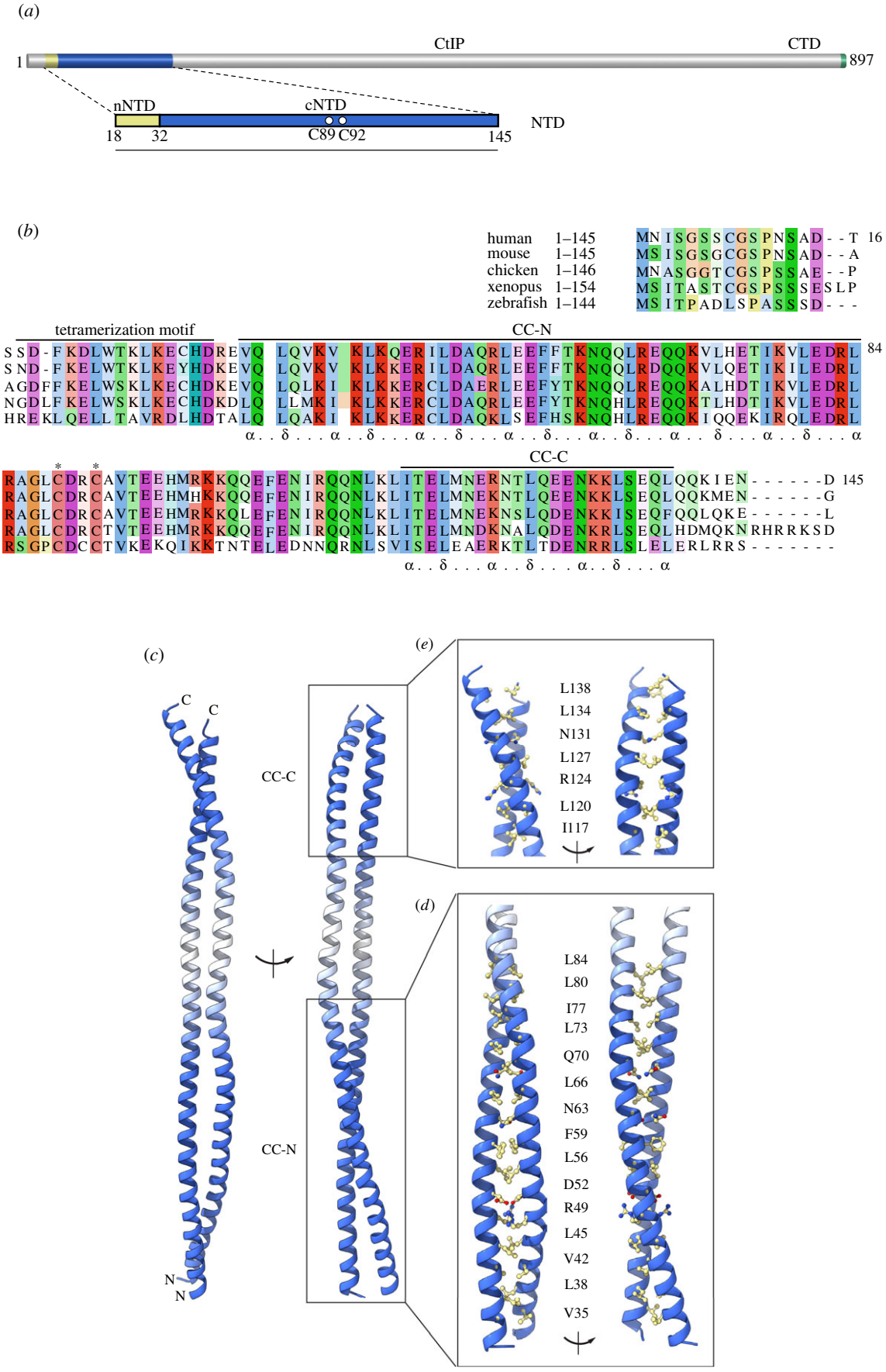

Figure 1. Coiled-coil structure of CtIP-cNTD. (*a*) The domain structure of human CtIP. The amino-terminal domain of CtIP (NTD) is comprised of an N-terminal sequence (nNTD), responsible for CtIP tetramerization, and a C-terminal coiled-coil sequence (cCTD) that includes a zinc-binding motif, with C89 and C92 as ligands. (*b*) Sequence conservation at the N-terminus of CtIP. The multiple sequence alignment is annotated to show the amino acid extent of CtIP's tetramerization motif and coiled-coil CC-N and CC-C segments. (*c*) Ribbon drawing of the crystal structure of the CtIP-cNTD. Two views of the structure related by a 90° rotation around its coiled-coil axis are shown. The coiled-coil regions of the structure are coloured in blue, while the intervening helical sequence is coloured in white. The N- and C-terminal coiled coils are labelled CC-N and CC-C, respectively. (*d*) Structural details of the CC-N. The side chains of interdigitating residues in the coiled coil are shown as the ball-and-stick models. Two rotated views are shown. (*e*) The same as in (*b*), but for the CC-C.

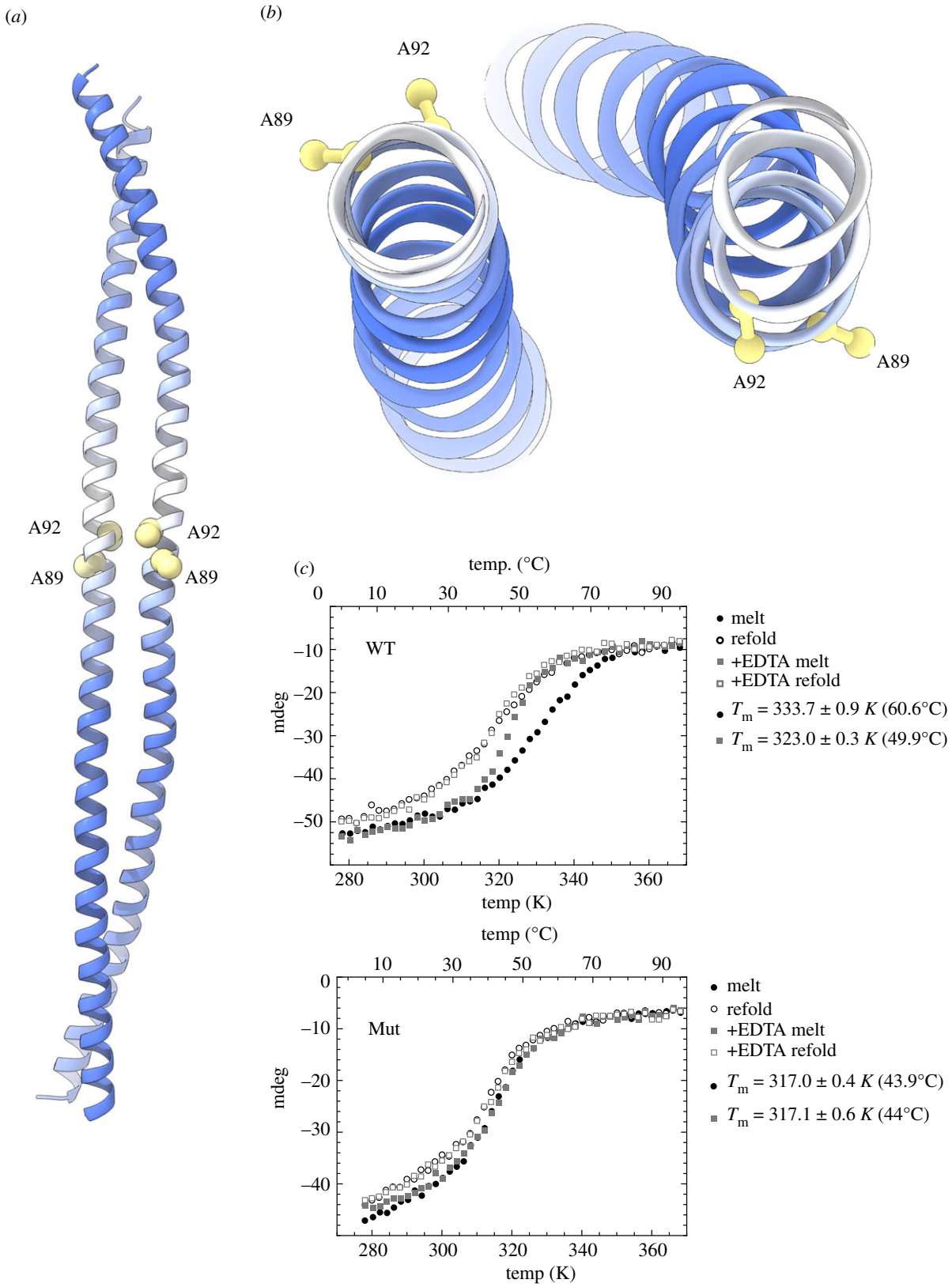

Figure 2. Characterization of the cNTD mutant. (*a*) Conformational consequence of the double C89A, C92A mutation. The position of the alanine residues is shown by drawing their side chains as spacefill models, while the rest of the structure is drawn as in figure 1. (*b*) Top view of the cNTD structure, highlighting the outwardly pointing side chains of A89 and A92. (*c*) Melting and refolding CD curves of wild-type (top) and C89A, C92A mutant cNTD (bottom), in the presence and absence of EDTA.

zinc ion by two CtIP chains, with the four cysteine ligands pointing inwardly towards the metal ion. Surprisingly, in the crystal structure, the alanine residues occupying the position of the zinc-binding cysteines 89 and 92 point outwardly towards the solvent (figure 2*a*), in a conformation that appears incompatible with the shared coordination of a zinc ion (figure 2*b*). The reason for this unexpected arrangement is unclear; it is possible that the presence of alpha helix-promoting alanine residues in the mutant protein had induced the formation of a local helical conformation, leading to the observed continuous alpha-helical structure for the entire CtIP-cNTD sequence.

2.2. CD analysis of CtIP-cNTD

We decided to explore the conformation of the wild-type and Mut CtIP-cNTD proteins using circular dichroism (CD) melting experiments. The CD analysis shows that the wild-type protein is considerably more stable than the mutant ($T_{m,WT} = 333.7$ K versus $T_{m,Mut} = 317.0$ K) (figure 2*c*), supporting a structural model where zinc cross-links two CtIP chains, thus conferring additional stability to the coiled-coil interactions of the protein dimer. In agreement with the model, treatment of the wild-type protein with the divalent ion-chelator EDTA reduced the $T_{m,WT}$ (323.0 K), while it had no significant effect on the $T_{m,Mut}$ (figure 2*c*). Interestingly, the refolding curve of wild-type CtIP-cNTD did not coincide with its melt curve (figure 2*c*), suggesting that its refolding is a complex process, as would be expected for a structure that contains a folded zinc-binding module in addition to the helical structure. By contrast, the melt and refold curves of the mutant CtIP-cNTD protein overlap, indicative of a simpler conformational transition between folded and unfolded states.

2.3. SAXS analysis of the CtIP-cNTD dimer

To investigate further the structure of CtIP-cNTD, we determined its size and shape by size-exclusion chromatography small-angle X-ray scattering (SEC-SAXS; referred to as SAXS here) (figure 3*a*; electronic supplementary material, table S2). SAXS analysis revealed cross-sectional radii (*Rc*) of 8.4 Å and 9.4 Å for wild-type and mutant proteins, respectively (electronic supplementary material, figure S2*a*,*b*), within the expected range for dimeric coiled-coils [28–30]. Furthermore, their interatomic distance distribution *P*(*r*) indicates the maximum dimensions of 170 Å and 180 Å, respectively (figure 3*b*), slightly longer than the length (160 Å) of the cNTD in the crystal. Fitting of the cNTD crystal structure to the SAXS data gave moderate fits, with χ^2 values of 6.94 (WT) and 3.89 (Mut), which were improved by flexible modelling of disordered residues at the termini of the crystallographic model (χ^2 of 5.08 and 2.75, respectively; figure 3*a*; electronic supplementary material, table S2). Thus, the wild-type and mutant CtIP-cNTD proteins in solution contain subtle structural differences relative to the crystal structure of the mutant CtIP-cNTD.

To gain insight into the solution conformation of the cNTD protein, we performed multi-phase SAXS *ab initio* modelling of wild-type and mutant CtIP-cNTD in MONSA [31]. The *ab initio* modelling demonstrated the end-on arrangement of the CC-N and CC-C regions, with a distinct obtuse angle at the junction between CC-N and CC-C, corresponding to the C89xxC92 site (figure 3*c*,*d*). This angle is more marked for the wild-type (120°) than the mutant protein (140°), suggesting that zinc coordination induces a kink to the cNTD structure that is reduced upon loss of zinc binding.

In parallel, we performed SAXS-directed modelling through a molecular dynamics (MD) approach using BilboMD [32], in which dimeric regions of amino acids 31–91 and 93–145 were defined as rigid domains within the cNTD model, with flexibility at the C89xxC92 site and the unstructured termini. The resultant models closely fitted the wild-type and mutant SAXS data, with χ^2 values of 1.18 and 1.13 (figure 3*a*), and demonstrated clear angulations at their C89xxC92 sites that are more marked in the wild-type (140°) than the mutant (110°) (figure 3*e*,*f*).

Both *ab initio* and MD modelling of the cNTD indicate that zinc coordination at the C89xxC92 site imposes a pronounced angle between the CC-N and CC-C segments of the cNTD, akin to a zinc-hinge. The loss of zinc-binding in the mutant likely disrupts this hinge conformation, allowing the near-linear helical conformation observed in the crystal structure of the cNTD mutant.

2.4. SAXS analysis of the CtIP-NTD tetramer

How does the zinc-hinge affect the conformation of the CtIP tetramer? In agreement with the model of CtIP-NTD as an elongated dimer-of-dimers, SAXS analysis of CtIP-NTD (18–145) revealed a cross-sectional radius *Rc* of 9.4 Å and a maximum dimension *P*(*r*) of 330 Å (figure 4*a*,*b*; electronic supplementary material, figure S3a,b and table S2), indicating a coiled-coil structure of almost twice the length of a single cNTD molecule. Furthermore, multi-phase SAXS *ab initio* modelling demonstrated the end-on arrangement of two angled cNTD molecules (figure 4*c*), consistent with the proposed head-to-head 'dimer-of-dimers' assembly.

The nNTD and cNTD crystal structures share amino acids 31–52, allowing two cNTD molecules to be docked onto one nNTD structure, thus generating a three-dimensional model of the CtIP-NTD (electronic supplementary material, figure S3*c*). Due to the presence of the kink caused by the zinc-binding motif in the middle of the cNTD, it was possible to generate CtIP-NTD models in either *cis* or *trans* configurations, with opposing cNTD molecules bending in the same or opposing directions. While linear CtIP-NTD models generated from the cNTD crystal structure fitted poorly the experimental SAXS data (figure 4*a*; $\chi^2 = 50.54$), fits were improved using angled CtIP-NTD models generated from the previously described cNTD molecular dynamics models (figure 4*a*; $\chi^2 = 17.80$). On this basis, we performed SAXS-directed molecular dynamics modelling from *cis* and *trans* CtIP-NTD models in which the central 18–88 tetramer and two 93–145 dimers were specified as rigid bodies, with flexibility allowed within the C89xxC92 site. The resultant *cis* and *trans* models closely fitted the experimental data (χ^2 values of 2.35 and 1.73; figure 4*a*) and revealed clear angulations at the zinc-hinge, resulting in CC-C coiled-coils that are orientated in the same or opposing directions (figure 4*d*,*e*).

This analysis suggests that the zinc-hinge generates CtIP-NTD structures in which opposing cNTD molecules can adopt either *cis* or *trans* conformations, according to the relative direction of bending at the zinc hinges of the two cNTDs in the CtIP tetramer. We speculate that these alternative conformations of the CtIP-NTD could play a role in mediating the appropriate tetrameric CtIP conformation in the presence of different DNA-end geometries.

2.5. Dynamic analysis of CtIP-cNTD conformation by diffracted X-ray tracking

To explore further the conformation of CtIP-cNTD, we performed a comparative analysis of wild-type and mutant CtIP-cNTD using diffracted X-ray tracking (DXT). DXT allows the sensitive detection of dynamic changes in the protein structure by tracking the X-ray diffraction spots of a

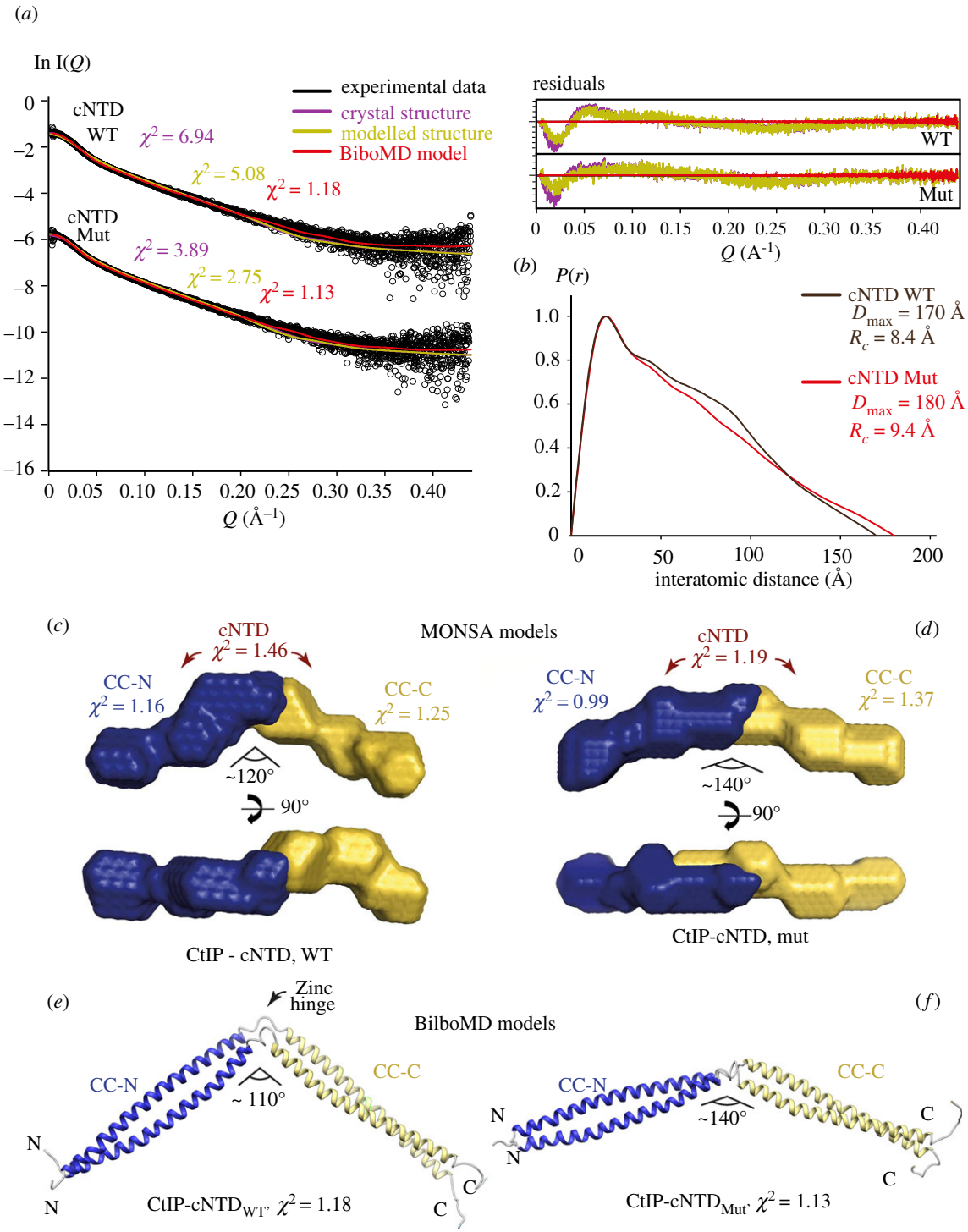

Figure 3. CtIP-cNTD contains a CxxC zinc-hinge. (*a*) SEC-SAXS analysis of wild-type and mutant cNTD. SAXS scattering data (black) are overlaid with the theoretical scattering curves of the crystal structure (purple), the crystal structure remodelled at its C-terminus (yellow) and BilboMD molecular dynamics models (red). Residuals for each fit are shown (inset). (*b*) Interatomic distance distributions of wild-type (green) and double-mutant (red) cNTD, showing the maximum dimensions of 170 Å and 180 Å, respectively. (*c*,*d*) Multi-phase SAXS *ab initio* (MONSA) models of wild-type and mutant cNTD, respectively, coloured blue (CC-N) and yellow (CC-C). χ^2 values for the entire envelope and individual phases are shown. (*e*,*f*) Molecular dynamics (BilboMD) models of wild-type and mutant cNTD, respectively, generated with CC-N and CC-C as rigid domains. Colour scheme as shown in (*c*,*d*).

gold nanocrystal covalently attached to the protein (figure 5*a*) [33]. The motion of the diffraction spot generates a track across the detector that can provide dynamic information on intra-molecular tilting (theta (θ) angle) and twisting (chi (χ) angle) motions of the protein, as well as information on relative domain mobility when structural information is available [34]. For the DXT experiment, CtIP-cNTD was immobilized on the surface of the experimental support by maleimide coupling, which guaranteed a high degree of support derivatization, and then labelled with gold nanocrystals. DXT experiments were performed using broadband synchrotron radiation, and a nanosecond, time-resolved photon-counting detector. DXT traces were collected for wild-type and mutant CtIP-cNTD (electronic supplementary material, figure S4*a*).

The analysis of the DXT data for wild-type and mutant CtIP-cNTD shows a more dynamic behaviour of the wild-type protein relative to the mutant protein (figure 5*b*;

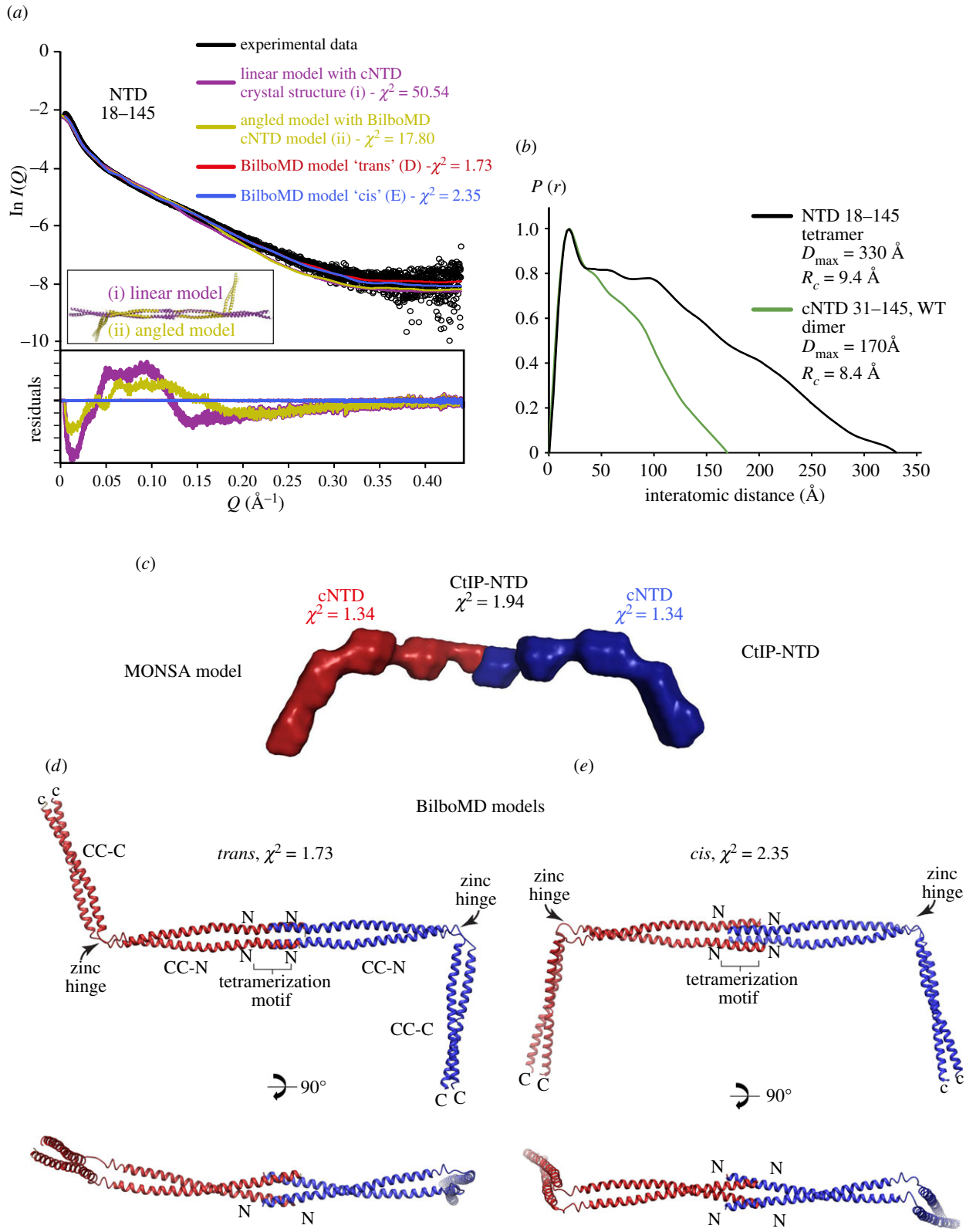

Figure 4. *Cis* or *trans* configurations of the CtIP-NTD tetramer. (*a*) SAXS analysis of CtIP-NTD (18–145). SAXS scattering data (black) overlaid with the theoretical scattering curves of linear (purple) and angled (yellow) models of the structure (shown in the inset), alongside BilboMD molecular dynamics models in *cis* (blue) and *trans* (red) configurations. Residuals for each fit are shown (inset). (*b*) Interatomic distance distribution of CtIP-NTD, showing the maximum dimensions of 300 Å. The distance distribution of CtIP-cNTD is shown in green for comparison. (*c*) Multi-phase *ab initio* (MONSA) model of the CtIP-NTD tetramer, consisting of two cNTD dimers, in red and blue envelopes. (*d*,*e*) Molecular dynamics (BilboMD) models of CtIP-NTD, generated with the 18–88 tetramer and two 93–145 dimers as rigid bodies, in *trans* and *cis* conformations.

electronic supplementary material, figures S4*b* and S5). In particular, the largest difference is in the theta angle distribution, which corresponds to a tilting motion of the structure (figure 5*c–e*). In the light of the known structural information for CtIP-cNTD, this difference in tilting dynamics can be interpreted as increased flexibility due to a hinge motion centred at the zinc-binding motif, present in the wild-type but not in the mutant protein. Thus, the DXT analysis supports the presence of a dynamic hinge motion enabled by the zinc-binding motif and expands our structural characterization of the CtIP-cNTD as an angular coiled-coil structure with a dynamic joint at its centre.

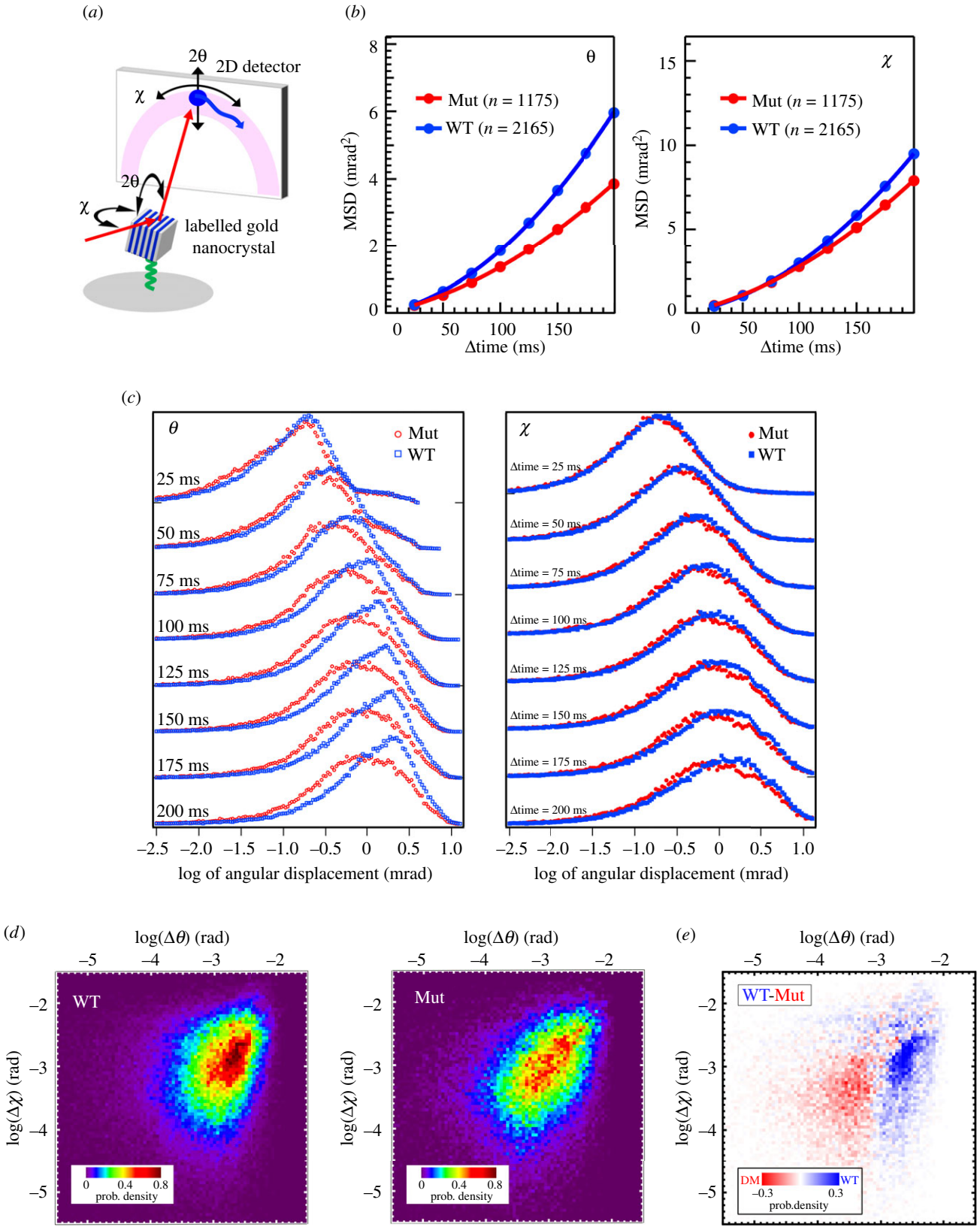

Figure 5. DXT analysis of CtIP-cNTD. (*a*) Schematic diagram of the set-up for a DXT experiment. (*b*) Mean square displacement (MSD) curves for the θ and χ angles. 'n' is the number of diffraction spots tracked from the labelled gold nanocrystals targeted for DXT analysis. (*c*) The time-resolved distributions of angular displacements over a period of 200 ms for θ and χ. (*d*) Two-dimensional histogram representation of the angular displacement distribution for θ at 200 ms (panel *c*). (*e*) Two-dimensional difference histogram between the angular displacement distribution of θ for WT and Mut, shown in panel (*d*).

3. Discussion

In this paper, we present two important advances concerning the molecular architecture of human CtIP. We have shown that its N-terminal domain exists predominantly as a parallel dimeric coiled-coil. We have further shown that the zinc-binding motif in the middle of the coiled-coil dimer introduces a structural discontinuity that imparts both a pronounced angulation and a distinct dynamic behaviour to the protein shape. These results expand considerably our experimental knowledge of the molecular architecture of CtIP, when considered together with our previous elucidation of the

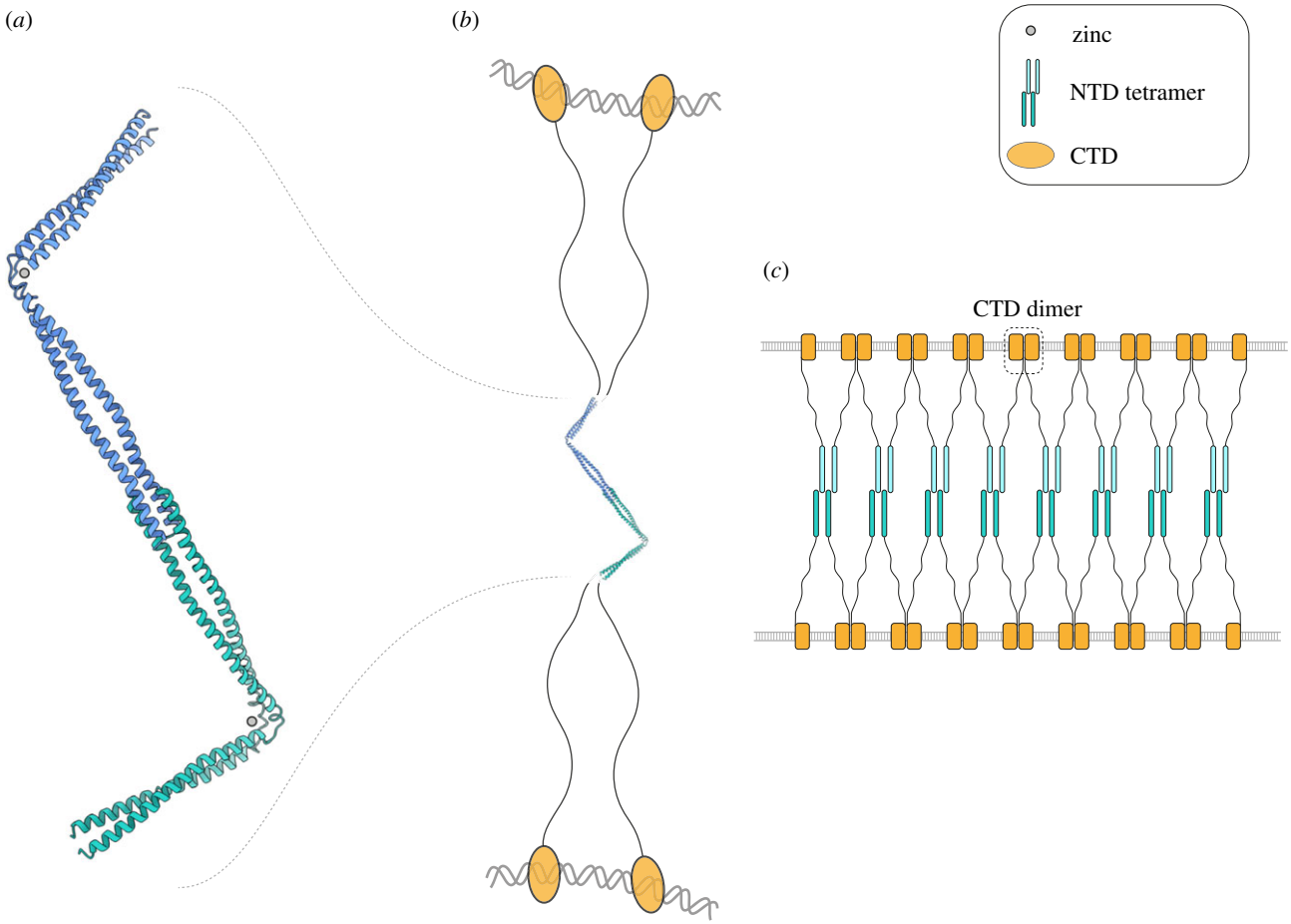

Figure 6. Model for the interaction of tetrameric CtIP with DNA. (*a*) Tetrameric architecture of the CtIP N-terminus, obtained by merging the crystal structures for the tetramerization motif and the dimeric coiled-coil region of CtIP. The cNTD has been modelled with a bent conformation at the zinc-binding motif, to reflect the interpretation of the SAXS analysis. The protein chains are drawn as ribbons and the two dimers are coloured in cyan and green. (*b*) The architecture of full-length CtIP. Such dimer-of-dimers arrangement of CtIP chains would allow bridging of distant DNA sites via DNA-binding of the C-terminal domains (CTDs). The CTDs are shown as orange ovals, connected to the N-terminal tetrameric structure by intrinsically disordered regions. (*c*) A model for the possible multimerization of CtIP on DNA. In the model, juxtaposed dimers of dimers would connect via the association of DNA-bound CTDs, potentially forming a protein network holding two DNA molecules together. The model is supported by recently published evidence of higher-order DNA-bound CtIP/Ctp1 structures [26,27] and the ability of CTD to dimerize (C.R.M. & L.P. 2019, unpublished observation).

structural basis for CtIP tetramerization and the published evidence for a dumbbell shape of human CtIP [25]. Thus, CtIP forms an extended dimer of dimers, where two parallel dimers of coiled-coil polypeptides tetramerize by intermeshing the N-end of their chains while projecting away from each other in opposing directions.

Such a tetrameric architecture confers upon CtIP the ability to bridge distant DNA sites, either on the same or on different chromosomes or sister chromatids, in agreement with its well-established functions in DNA DSB repair and meiosis (figure 6). We note that the head-to-head dimer-of-dimers architecture of CtiP is strikingly reminiscent of the tetrameric architecture of synaptonemal complex protein SYCP1 [30]. During prophase I of meiosis, SYCP1 directs the close pairing of meiotic chromosomes, cross-linking parental chromosomes by virtue of an extended self-assembly mechanism driven by the dimer-of-dimers interactions of its helical N-termini. It is possible that CtIP might adopt a similar mechanism to hold together DNA ends in preparation for end resection. Thus, the use of an extended architecture based on the head-to-head association of dimeric helical coiled coils might be a general way to hold together distant nucleic-acid segments during metabolic processes that require recombination between homologous DNA molecules.

The role of the zinc-binding motif in such a mechanistic model of CtIP has remained unclear, as it is not required for CtIP-cNTD dimerization and no biochemical function, such as DNA binding, has been attributed to it; equally, no evidence for a putative function is available from cellular assays. Our data provides structural insight into the zinc-binding motif, by showing that its presence induces a marked angulation in the shape of the CtIP-cNTD. The consequence of such conformational effect on the coiled coil of the cNTD is that two different tetrameric architectures of CtIP can be envisioned; these can be purposefully named *cis* and *trans* according to whether the C-termini of the CtIP-NTD are found on the same side or opposite sides of the long two-fold symmetry axis of the tetramer.

The functional implications of the existence of two distinct arrangements for the CtIP-NTD are presently unclear. It is possible that the geometry of the DNA sites influences the protein conformation, so that a *cis* conformation might be selected in the case of a single DSB, whereas a *trans* conformation is adopted when holding onto pairs of sister chromatids. The fact that the majority of the CtIP protein beyond the NTD appears to be intrinsically unstructured highlights how such simple geometric models remain highly tentative. A deeper mechanistic understanding of CtIP function in DNA DSB repair will require high-resolution studies of the full-length protein, in isolation and bound within the end-resection complexes of HR.

4. Material and methods

4.1. Recombinant-protein expression and purification

Sequences corresponding to human CtIP residues 18–145, 31–145, 31–88 and 91–145, including 31–145 double-mutant C89A C92A, were cloned into pMAT11 vectors for expression as N-terminal His_6-MBP fusion proteins with the addition of a Strep tag at the C-terminus. Constructs were expressed in BL21(DE3) Rosetta 2 cells (Novagen) in 2xYT medium, after induction with 0.5 mM IPTG for 16 h at 20°C. Fusion proteins were purified from the clarified lysate by Ni-NTA (Qiagen) affinity chromatography. The His-MBP tag was removed by cleavage with TEV protease (Invitrogen). Further purification was achieved through the capture of the cleaved protein by Strep-Tactin resin (IBA) and elution with 2.5 mM *d*-desthiobiotin (Sigma). A final purification step was performed by size-exclusion chromatography using a HiLoad 16/60 Superdex 75 column (GE Healthcare) in 20 mM Tris HCl pH 8.0, 300 mM NaCl. Fractions containing pure CtIP protein were concentrated to 10 mg ml^{-1} and stored at −80°C after flash freezing in liquid nitrogen.

4.2. Circular dichroism spectroscopy

Far-UV CD spectroscopy data were collected on an Aviv 410 spectropolarimeter (Biophysics Facility, Department of Biochemistry, University of Cambridge). CtIP samples were analysed at 0.2 mg ml^{-1}, in 5 mM Na_2HPO_4/NaH_2PO_4, pH 8.0 and 100 mM NaF, with a quartz cuvette with 1-mm path length. CD thermal denaturation data were recorded at 222 nm, at 2°C intervals between 5 and 95°C (1°C/minute ramping rate, with 30-s incubation time). The data were fitted to a rearrangement of the Gibbs–Helmholtz relationship [35,36] using pro Fit software (Quantum Soft).

4.3. Size-exclusion chromatography multi-angle light scattering (SEC-MALS)

The absolute molecular masses of recombinant CtIP protein samples were determined by SEC-MALS. 100-µl protein samples (at approximately 2 mg ml^{-1}) were loaded onto a Superdex 200 or 75 10/300 GL Increase size-exclusion chromatography column (GE Healthcare) in 20 mM Tris HCl, pH 8.0, 300 mM NaCl, with or without 2 mM EDTA, at 0.5 ml min^{-1} with an ÄKTA Purifier (GE Healthcare). The column output was fed into a DAWN HELEOS II MALS detector (Wyatt Technology) followed by an Optilab T-rEX differential refractometer (Wyatt Technology). Light scattering (LS) and differential refractive index (dRI) data were collected and analysed with ASTRA 6 software (Wyatt Technology). Molecular masses and estimated errors were calculated across individual eluted peaks by extrapolation from Zimm plots with a dn/dc value of 0.1850 ml g^{-1}. SEC-MALS data are presented with LS and dRI plotted alongside fitted molecular masses (Mr).

4.4. Protein crystallization and X-ray structure solution

Initial crystallization hits for the 31–145 DM CtIP protein were observed with condition F6 of the Morpheus commercial screen MD-47 (Molecular Dimensions). Crystals were improved by hanging-drop vapour diffusion and micro-seeding, mixing the protein sample at 7.5 mg ml^{-1} with crystallization buffer and micro seed sample at a ratio of 10 : 19 : 1. X-ray diffraction data were collected at wavelength 0.976251 Å, 100 K as 990 contiguous frames with 0.02 s exposure and 0.1° oscillation on a Pilatus3_6 M detector at beamline ID30B of the ESRF Grenoble, France. The diffraction images were indexed and intensities extracted and scaled in XDS [37] and further scaled and analysed using Aimless [38]. Crystals were assigned to the trigonal $P3_2$ space group with unit cell dimensions: $a = b =$ 86.6 Å, $c = 42.6$ Å, $\alpha = \beta = 90$, $\gamma = 120$, with one protein dimer in the asymmetric unit. The crystal structure was solved by MR using Phaser [39]. Two helical coiled-coil models spanning amino acids 56–83 and 99–144 of human CtIP, corresponding to the regions of CtIP-NTD strongly predicted to form coiled-coil structures, were generated in CBuilder2.0 [40] and used as search templates. The use of idealized coiled-coil models as search templates is now well established in MR software such as AMPLE [41,42]. Phaser successfully placed both models in the asymmetric unit, with no model clashes and a clear indication of extra electron density for the missing parts of the crystallographic model (electronic supplementary material, figure S1). An initial poly-alanine model was refined in Phenix [43], adding side chains and extending the model to boundaries of the interpretable density maps. Refinement in Phenix was interspersed with manual rebuilding in Coot [44], to improve fitting to the electron density map and the stereochemistry of the model. The refined crystallographic model of the human CtIP-NTD comprises amino acids 31 to 136 for both chains, with $R_{work}/R_{free} = 0.2528/2235$, no Ramachandran outliers and an overall Molprobity score of 1.05 [45].

4.5. Size-exclusion chromatography small-angle X-ray scattering (SEC-SAXS)

SEC-SAXS experiments were performed at the bioSAXS beamline B21 (Diamond Light Source synchrotron, UK). Protein samples at concentrations in the range 3–10 mg ml^{-1} were analysed using a Superdex 200 Increase 3.2/300 2.4 ml column in 20 mM Tris HCl 8.0, 300 mM NaCl at 0.05 ml min^{-1} in an Agilent 1200 HPLC system. The column outflow passed through the experimental cell, where SAXS data were recorded at 12.4 keV, detector distance 4.014 m, in 3.0 s frames. ScÅtter 3.0 (http://www.bioisis.net) was used to subtract, average and carry out Guinier analysis for the *Rg* and cross-sectional *Rg* (*Rc*), and *P*(*r*) distributions were fitted using PRIMUS [46]. Multi-phase SAXS *ab initio* modelling was performed using MONSA [31]; rigid-body and flexible tail modelling were performed using CORAL [47]. Molecular dynamics modelling against experimental SAXS data was performed using BilboMD [32] (https://bl1231.als.lbl.gov/bilbomd), with regions 18–88 or 31–88 and 93–145 specified as rigid bodies. Crystal structures and models were fitted to experimental data using CRYSOL [48].

4.6. Structural modelling

Structural modelling and visualization were performed using Coot [44] and PyMOL Molecular Graphics System, v. 2.3 Schrödinger, LLC. The CtIP-cNTD C-terminus was modelled as an ideal coiled-coil using CCBuilder 2.0 [40] (http://coiledcoils.chm.bris.ac.uk/ccbuilder2/builder), docked onto

the cNTD crystal structure and used to replace the deviating terminus of chain A (amino acids 122–138) and to extend chain B to amino acid 145. The tetrameric CtIP-NTD structure was modelled by docking two copies of the cNTD onto the nNTD crystal structure [21] (PDB ID 4D2H) based on the shared structure of amino acids 31–52 (RMS deviation = 0.413). Models were generated in *cis* or *trans* configurations by docking cNTD structures with their asymmetric bends in the same or opposing directions, respectively. Linear models were generated from the cNTD double-mutant crystal structure, whereas angled models were generated using the angled cNTD structure that was obtained from BilboMD molecular dynamics modelling against experimental CtIP-cNTD wild-type SAXS data.

4.7. Diffracted X-ray tracking

A Kapton (Polyimide film, DuPont) surface was pre-treated with UV radiation for 1/6 h to generate a negatively charged surface for poly-lysine (0.01% W/V) coating. To this, GMBS (N-(4-Maleimidobutyryloxy) succinimide (Dojindo Laboratories)) was bound to the poly-lysine-coated surface. For sufficient CtIP-cNTD coverage, CtIP-cNTD was applied to the GMBS-coated surface in excess and incubated at 4°C for 1/6 h. Gold nanocrystals were pre-treated with 10-Carboxy-1-decanethiol (Dojindo Laboratories) to prevent aggregation and modify the gold surface for both methionine and cysteine coupling to CtIP-cNTD. This was subsequently incubated with the protein surface for 1/6 h at 4°C followed by washing into the protein buffer and sealing within the apparatus for exposure to the X-ray beam.

DXT experiments were performed at the B16 beamline of the Diamond Light Source synchrotron (UK). The CtIP-cNTD samples were irradiated with X-rays with energy bandwidths ranging from 11 to 17 keV and with a beam size of 0.5 mm diameter, and diffraction movies were recorded by a Tristan 1 M detector with 16 timepix3 chips located 120 mm from the sample. All diffracted photon hits on the detector were recorded and time-resolved diffraction images (25 ms f^{-1}) were reconstructed with the software provided by the detector group at the Diamond Light Source. An incident X-ray irradiated one position of the sample for 3 s, and the same measurement was repeated at 50 different sample positions on each sample. The motions of the spots diffracted from the gold nanocrystals on the substrate's surface were tracked by TrackPy (v. 0.4.2 https://doi.org/10.5281/zenodo.3492186), and the trajectories of the diffraction spots (electronic supplementary material, figure S3*a*) were analysed using custom software written within IGOR Pro (Wavemetrics, Lake Oswego, OR). The motionless diffracted spots, less than 1 mrad in the theta direction, and the events on the edge pixels in each Timepix3 chip were excluded for the analysis.

Data accessibility. Coordinates and structure factors for CtIP-cNTD have been deposited in the Protein Data Bank with access code 7BGF.

Authors' contributions. C.R.M. carried out all experimental work, assisted by N.J.R. (protein preparation), J.D.M. (CD experiments), R.R. (SAXS experiments); O.R.D. performed the analysis of the SAXS data. C.R.M. and Y.C.S. performed the DXT experiments and Y.C.S., assisted by M.K. and H.S., analysed the DXT data. L.P. conceived and supervised the project and wrote the manuscript with input from all authors.

Competing interests. We declare we have no competing interests.

Funding. This work was funded by the Wellcome Trust investigator award 104641/Z/14/Z to L.P. O.R.D. is a Wellcome Trust Senior Research Fellow (grant no. 219413/Z/19/Z).

Acknowledgements. We would like to thank the beamline staff of the Diamond Light Source (Nathan Cowieson, David Omar, Giulio Crevatin, William Nichols, Alan Greer, Nicola Tartoni) for help with SAXS and DXT data collection. We would further like to thank Katsuaki Inoue and Oliver Fox at Diamond Light Source for help with the DXT measurements.

References

1. Ciccia A, Elledge SJ. 2010 The DNA damage response: making it safe to play with knives. *Mol. Cell* **40**, 179–204. (doi:10.1016/j.molcel.2010.09.019)
2. Jackson SP, Bartek J. 2009 The DNA-damage response in human biology and disease. *Nature* **461**, 1071–1078. (doi:10.1038/nature08467)
3. Pannunzio NR, Watanabe G, Lieber MR. 2018 Nonhomologous DNA end-joining for repair of DNA double-strand breaks. *J. Biol. Chem.* **293**, 10 512–10 523. (doi:10.1074/jbc.tm117.000374)
4. Wright WD, Shah SS, Heyer W-D. 2018 Homologous recombination and the repair of DNA double-strand breaks. *J. Biol. Chem.* **293**, 10 524–10 535. (doi:10.1074/jbc.tm118.000372)
5. Scully R, Panday A, Elango R, Willis NA. 2019 DNA double-strand break repair-pathway choice in somatic mammalian cells. *Nat. Rev. Mol. Cell Biol.* **20**, 698–714. (doi:10.1038/s41580-019-0152-0)
6. Ronato DA, Mersaoui SY, Busatto FF, Affar EB, Richard S, Masson J-Y. 2020 Limiting the DNA double-strand break resectosome for genome protection. *Trends Biochem. Sci.* **45**, 779–793. (doi:10.1016/j.tibs.2020.05.003)
7. Her J, Bunting SF. 2018 How cells ensure correct repair of DNA double-strand breaks. *J. Biol. Chem.* **293**, 10 502–10 511. (doi:10.1074/jbc.tm118.000371)
8. You Z, Bailis JM. 2010 DNA damage and decisions: CtIP coordinates DNA repair and cell cycle checkpoints. *Trends Cell Biol.* **20**, 402–409. (doi:10.1016/j.tcb.2010.04.002)
9. Makharashvili N, Paull TT. 2015 CtIP: a DNA damage response protein at the intersection of DNA metabolism. *DNA Repair* **32**, 75–81. (doi:10.1016/j.dnarep.2015.04.016)
10. Yun MH, Hiom K. 2009 CtIP-BRCA1 modulates the choice of DNA double-strand-break repair pathway throughout the cell cycle. *Nature* **459**, 460–463. (doi:10.1038/nature07955)
11. Huertas P, Cortés-Ledesma F, Sartori AA, Aguilera A, Jackson SP. 2008 CDK targets Sae2 to control DNA-end resection and homologous recombination. *Nature* **455**, 689–692. (doi:10.1038/nature07215)
12. Anand R, Ranjha L, Cannavo E, Cejka P. 2016 Phosphorylated CtIP functions as a co-factor of the MRE11-RAD50-NBS1 endonuclease in DNA end resection. *Mol. Cell* **64**, 940–950. (doi:10.1016/j.molcel.2016.10.017)
13. Cannavo E, Cejka P. 2014 Sae2 promotes dsDNA endonuclease activity within Mre11-Rad50-Xrs2 to resect DNA breaks. *Nature* **514**, 122–125. (doi:10.1038/nature13771)
14. Przetocka S *et al.* 2018 CtIP-mediated fork protection synergizes with BRCA1 to suppress genomic instability upon DNA replication stress. *Mol. Cell* **72**, 568–582.e6. (doi:10.1016/j.molcel.2018.09.014)
15. Zarrizi R *et al.* 2020 Germline RBBP8 variants associated with early-onset breast cancer compromise replication fork stability. *J. Clin. Invest.* **130**, 4069–4080. (doi:10.1172/jci127521)
16. Mohiuddin M, Rahman MM, Sale JE, Pearson CE. 2019 CtIP-BRCA1 complex and MRE11 maintain replication forks in the presence of chain

terminating nucleoside analogs. *Nucl. Acids Res.* **47**, gkz009. (doi:10.1093/nar/gkz009)
17. Dubin MJ *et al.* 2004 Dimerization of CtIP, a BRCA1- and CtBP-interacting protein, is mediated by an N-terminal coiled-coil motif. *J. Biol. Chem.* **279**, 26 932–26 938. (doi:10.1074/jbc.m313974200)
18. Wang H, Shao Z, Shi LZ, Hwang PY-H, Truong LN, Berns MW, Chen DJ, Wu X. 2012 CtIP protein dimerization is critical for its recruitment to chromosomal DNA double-stranded breaks. *J. Biol. Chem.* **287**, 21 471–21 480.
19. Yuan J, Chen J. 2009 N terminus of CtIP is critical for homologous recombination-mediated double-strand break repair. *J. Biol. Chem.* **284**, 31 746–31 752. (doi:10.1074/jbc.m109.023424)
20. Sartori AA, Lukas C, Coates J, Mistrik M, Fu S, Bartek J, Baer R, Lukas J, Jackson SP. 2007 Human CtIP promotes DNA end resection. *Nature* **450**, 509–514. (doi:10.1038/nature06337)
21. Davies OR *et al.* 2015 CtIP tetramer assembly is required for DNA-end resection and repair. *Nat. Struct. Mol. Biol.* **22**, 150–157. (doi:10.1038/nsmb.2937)
22. Andres SN, Appel CD, Westmoreland JW, Williams JS, Nguyen Y, Robertson PD, Resnick MA, Williams RS. 2015 Tetrameric Ctp1 coordinates DNA binding and DNA bridging in DNA double-strand-break repair. *Nat. Struct. Mol. Biol.* **22**, 158–166. (doi:10.1038/nsmb.2945)
23. Wang H *et al.* 2013 The interaction of CtIP and Nbs1 connects CDK and ATM to regulate HR-mediated double-strand break repair. *PLoS Genet.* **9**, e1003277. (doi:10.1371/journal.pgen.1003277)
24. Williams RS *et al.* 2009 Nbs1 flexibly tethers Ctp1 and Mre11-Rad50 to coordinate DNA double-strand break processing and repair. *Cell* **139**, 87–99. (doi:10.1016/j.cell.2009.07.033)
25. Wilkinson OJ, Martín-González A, Kang H, Northall SJ, Wigley DB, Moreno-Herrero F, Dillingham MS. 2019 CtIP forms a tetrameric dumbbell-shaped particle which bridges complex DNA end structures for double-strand break repair. *eLife* **8**, e42129. (doi:10.7554/elife.42129)
26. Andres SN, Li ZM, Erie DA, Williams RS. 2019 Ctp1 protein–DNA filaments promote DNA bridging and DNA double-strand break repair. *J. Biol. Chem.* **294**, 3312–3320. (doi:10.1074/jbc.ra118.006759)
27. Öz R, Howard SM, Sharma R, Törnkvist H, Ceppi I KKS, Kristiansson E, Cejka P, Westerlund F. 2020 Phosphorylated CtIP bridges DNA to promote annealing of broken ends. *Proc. Natl. Acad. Sci. USA* **117**, 21 403–21 412. (doi:10.1073/pnas.2008645117)
28. Dunne OM, Davies OR. 2019 A molecular model for self-assembly of the synaptonemal complex protein SYCE3. *J. Biol. Chem.* **294**, 9260–9275. (doi:10.1074/jbc.ra119.008404)
29. Dunne OM, Davies OR. 2019 Molecular structure of human synaptonemal complex protein SYCE1. *Chromosoma* **14**, 1–14. (doi:10.1007/s00412-018-00688-z)
30. Dunce JM, Dunne OM, Ratcliff M, Millán C, Madgwick S, Usón I, Davies OR. 2018 Structural basis of meiotic chromosome synapsis through SYCP1 self-assembly. *Nat. Struct. Mol. Biol.* **7**, 1. (doi:10.1038/s41594-018-0078-9)
31. Svergun DI. 1999 Restoring low resolution structure of biological macromolecules from solution scattering using simulated annealing. *Biophys. J.* **76**, 2879–2886. (doi:10.1016/s0006-3495(99)77443-6)
32. Pelikan M, Hura G, Hammel M. 2009 Structure and flexibility within proteins as identified through small angle X-ray scattering. *Gen. Physiol. Biophys.* **28**, 174–189. (doi:10.4149/gpb_2009_02_174)
33. Sasaki YC, Suzuki Y, Yagi N, Adachi S, Ishibashi M, Suda H, Toyota K, Yanagihara M. 2000 Tracking of individual nanocrystals using diffracted X rays. *Phys. Rev. E* **62**, 3843–3847. (doi:10.1103/physreve.62.3843)
34. Sekiguchi H, Sasaki YC. 2019 Dynamic 3D visualization of active protein's motion using diffracted X-ray tracking. *Jpn. J. Appl. Phys.* **58**, 120501. (doi:10.7567/1347-4065/ab56fd)
35. Jackson SE, Fersht AR. 1991 Folding of chymotrypsin inhibitor 2. 1. Evidence for a two-state transition. *Biochemistry* **30**, 10 428–10 435. (doi:10.1021/bi00107a010)
36. Nicholson EM, Scholtz JM. 1996 Conformational stability of the *Escherichia coli* HPr protein: test of the linear extrapolation method and a thermodynamic characterization of cold denaturation. *Biochemistry* **35**, 11 369–11 378. (doi:10.1021/bi960863y)
37. Kabsch W. 2010 XDS. *Acta Crystallogr. D Biol. Crystallogr.* **66**, 125–132. (doi:10.1107/s0907444909047337)
38. Evans PR, Murshudov GN. 2013 How good are my data and what is the resolution? *Acta Crystallogr. D Biol. Crystallogr.* **69**, 1204–1214. (doi:10.1107/s0907444913000061)
39. McCoy AJ, Grosse-Kunstleve RW, Adams PD, Winn MD, Storoni LC, Read RJ. 2007 Phaser crystallographic software. *J. Appl. Crystallogr.* **40**, 658–674. (doi:10.1107/s0021889807021206)
40. Wood CW, Woolfson DN. 2018 CCBuilder 2.0: powerful and accessible coiled-coil modeling. *Protein Sci.* **27**, 103–111. (doi:10.1002/pro.3279)
41. Thomas JMH, Keegan RM, Rigden DJ, Davies OR. 2020 Extending the scope of coiled-coil crystal structure solution by AMPLE through improved ab initio modelling. *Acta Crystallogr. D* **76**, 272–284. (doi:10.1107/s2059798320000443)
42. Thomas JMH, Keegan RM, Bibby J, Winn MD, Mayans O, Rigden DJ. 2015 Routine phasing of coiled-coil protein crystal structures with AMPLE. *IUCrJ.* **2**, 198–206. (doi:10.1107/s2052252515002080)
43. Adams PD *et al.* 2010 PHENIX: a comprehensive Python-based system for macromolecular structure solution. *Acta Crystallogr. D Biol. Crystallogr.* **66**, 213–221. (doi:10.1107/s0907444909052925)
44. Emsley P, Cowtan K. 2004 Coot: model-building tools for molecular graphics. *Acta Crystallogr. D Biol. Crystallogr.* **60**, 2126–2132.
45. Davis IW *et al.* 2007 MolProbity: all-atom contacts and structure validation for proteins and nucleic acids. *Nucl. Acids Res.* **35**, W375–W383. (doi:10.1093/nar/gkm216)
46. Konarev PV, Volkov VV, Sokolova AV, Koch MHJ, Svergun DI. 2003 PRIMUS: a Windows PC-based system for small-angle scattering data analysis. *J. Appl. Crystallogr.* **36**, 1277–1282. (doi:10.1107/s0021889803012779)
47. Petoukhov MV *et al.* 2012 New developments in the ATSAS program package for small-angle scattering data analysis. *J. Appl. Crystallogr.* **45**, 342–350. (doi:10.1107/s0021889812007662)
48. Svergun D, Barberato C, Koch MHJ. 1995 CRYSOL: a program to evaluate X-ray solution scattering of biological macromolecules from atomic coordinates. *J. Appl. Crystallogr.* **28**, 768–773. (doi:10.1107/s0021889895007047)